CrossMark

Mid-Term Quasi-Periodicities and Solar Cycle Variation of the White-Light Corona from 18.5 Years (1996.0 – 2014.5) of LASCO Observations

T. Barlyaeva[1] · P. Lamy[1] · A. Llebaria[1]

Abstract We report on the analysis of the temporal evolution of the solar corona based on 18.5 years (1996.0 – 2014.5) of white-light observations with the SOHO/LASCO-C2 coronagraph. This evolution is quantified by generating spatially integrated values of the K-corona radiance, first globally, then in latitudinal sectors. The analysis considers time series of monthly values and 13-month running means of the radiance as well as several indices and proxies of solar activity. We study correlation, wavelet time-frequency spectra, and cross-coherence and phase spectra between these quantities. Our results give a detailed insight on how the corona responds to solar activity over timescales ranging from mid-term quasi-periodicities (also known as quasi-biennial oscillations or QBOs) to the long-term 11 year solar cycle. The amplitude of the variation between successive solar maxima and minima (modulation factor) very much depends upon the strength of the cycle and upon the heliographic latitude. An asymmetry is observed during the ascending phase of Solar Cycle 24, prominently in the royal and polar sectors, with north leading. Most prominent QBOs are a quasi-annual period during the maximum phase of Solar Cycle 23 and a shorter period, seven to eight months, in the ascending and maximum phases of Solar Cycle 24. They share the same properties as the solar QBOs: variable periodicity, intermittency, asymmetric development in the northern and southern solar hemispheres, and largest amplitudes during the maximum phase of solar cycles. The strongest correlation of the temporal variations of the coronal radiance – and consequently the coronal electron density – is found with the total magnetic flux. Considering that the morphology of the solar corona is also directly controlled by the topology of the magnetic field, this correlation reinforces the view that they are intimately connected, including their variability at all timescales.

✉ T. Barlyaeva
tatiana.barlyaeva@lam.fr

P. Lamy
philippe.lamy@lam.fr

A. Llebaria
antoine.llebaria@lam.fr

[1] Laboratoire d'Astrophysique de Marseille, UMR 7326, CNRS/Aix-Marseille Université, 38 rue Frédéric Joliot-Curie, 13388 Marseille cedex 13, France

1. Introduction

The variability of the solar white-light corona and its connection to the solar activity was probably first perceived after comparing several eclipse observations depicting different morphology at different phases of solar activity. Essentially, a flat streamer belt, characteristic of a corona during the minima, widens out to reach higher latitude regions together with the emergence of new structures that are later known as pseudo- and polar streamers. Following the progress made in the photometric analysis of the corona, the temporal variation of its total brightness was further investigated, leading to the widely accepted view that it increases from solar minimum to maximum, see the historical review of Fisher and Sime (1984), which covers the interval 1947 to 1984 and the updated list of available results in Table 1. The photometric variations between the minimum and maximum radiances of the corona that are known as the modulation factor reported in this table are not always strictly correct in the case of eclipses since they may have taken place at some intermediate stage of the solar cycle. These factors were determined using either the global K+F corona or the K-corona alone, and this may introduce a bias because the stable F component tends to reduce the variation by an amount that in addition depends upon the distance to the Sun. Eclipse observers generally compare their results with those of past eclipses that were often obtained with different techniques of observations, of data reduction, of absolute calibration, and under different sky conditions, to mention the most important effects that may affect the comparison. Finally, the time sampling allowed by eclipses is quite limited, typically a few years.

Partly alleviating these limitations, the 18-year long record of K-coronameter data from the Mauna Loa, Hawaii instruments analyzed by Fisher and Sime (1984) to determine the

Table 1 Summary of past results on the variability of the solar corona.

Authors	Observations	Coronal quantities	Time interval	Solar cycle	Modulation factor
Nikonov and Nikonova (1947)	Eclipses	K+F	1918 – 1945	15 – 18	2
Saito (1950)	Eclipse	K+F	1948	18	2[a]
van de Hulst (1950)	Eclipses	K+F	1893 – 1932	13 – 16	1.84
Abbott (1955)	Eclipses	K+F	1914 – 1945	15 – 18	2.1[b]
Waldmeier (1955)	Eclipses	K+F	1952, 1954	18 – 19	1.7[c]
Sytinskaya and Sharonov (1983)	Eclipses	K+F	1936 – 1961	17 – 19	No[d]
Fisher and Sime (1984)	K-coronameter	pB	1965 – 1983	20 – 21	2
Lebecq, Koutchmy, and Stellemacher (1985)	Eclipse	K	1981	21	4[a]
Llebaria, Lamy, and Koutchmy (1999)	LASCO	K	1996 – 1999	23	[e]
Lamy, Llebaria, and Quémerais (2002)	LASCO	K	1996 – 2002	23	4

[a]Values obtained by comparing the observed eclipse with the results of other authors at previous eclipse(s).

[b]Typical value at 2.7 $R_\odot$, decreasing beyond.

[c]Factor based on only two eclipses.

[d]No variation found.

[e]Not enough data.

variation of the monthly averages of the integrated polarized brightness pB of the corona led to a linear variation with sunspot number and a modulation factor of 2 at reference heights of 1.3 and 1.5 $R_\odot$ between the minimum and maximum of the activity cycle. These authors attempted to explain the origin of this variation in terms of the varying extent of the coronal holes without much success, and unfortunately did not explore additional variabilities.

Space coronagraphy is most appropriate to tackle the question of the temporal evolution of the corona, alleviating all shortcomings mentioned above, but none of the instruments flown on past long missions, *Skylab*, *Solwind*, and *Solar Maximum Mission* (SMM), had the required photometric performances. In contrast, the *Large Angle Spectrometric COronagraph* (LASCO; Brueckner *et al.*, 1995) with its superior sensitivity, excellent photometric performances, and record longevity is fully adapted to the quantitative analysis of the white-light corona over a long period of time and particularly its connection to the solar cycle. Llebaria, Lamy, and Koutchmy (1999) and Lamy, Llebaria, and Quémerais (2002) have already considered this question, but on a limited time frame (seven years of data for the second article) and have shown that the integrated radiance of the K-corona and its global electron content follow the solar cycle pattern very well that is for instance given by the sunspot number. Later on, Lamy *et al.* (2014) extended the analysis to 17 years (1996 – 2012) of LASCO-C2 data and concentrated on the comparison of the solar activity minima of Solar Cycles 22/23 and 23/24.

The present article is a generalization of this work as it addresses in detail the question of the temporal variation of the radiance of the K-corona based on 18.5 years (1996 – 2014.5) of LASCO-C2 observations. It is organized as follows. Section 2 presents the LASCO-C2 images and their processing as well as the solar proxies selected for comparison with the coronal activity. Section 3 describes the integration procedure of the radiance in an annulus extending from 2.7 to 5.5 $R_\odot$, first globally and then in different latitudinal sectors; it further describes the spectral and correlation analysis based on the wavelet method. In Section 4, we broadly characterize the temporal evolution of the radiance (global and in sectors), determine the modulation factors, and then analyze in detail the short-term variations and their north–south asymmetry. Section 5 is devoted to the comparison of coronal and solar activities at different timescales, solar cycle and short-term. Finally, we discuss our results in Section 6 and summarize them in Section 7.

2. Experimental Data

2.1. Coronal Radiance: LASCO-C2 Data

C2 is one of the two externally occulted coronagraphs of LASCO that has been in nearly continuous operation since January 1996 (Brueckner *et al.*, 1995). With its field of view extending from 2.2 to 6.5 $R_\odot$, it records the brightest part of the corona accessible to LASCO, and its images are therefore well suited to investigate its temporal variation. The operation of LASCO observations has experienced minor interruptions since 1996 for various instrumental and spacecraft reasons except from 25 June to 22 October 1998, when the SOHO spacecraft lost its pointing; normal operations only resumed in March 1999. Following Lamy *et al.* (2014), the present analysis makes use of the routine polarization sequences since their temporal cadence (typically one per day) is sufficient for our purpose and since they allow extracting the K-corona following a classical procedure. A polarization sequence

is composed of three linear polarized images of the corona obtained with three polarizers oriented at 60°, 0°, and −60° and an unpolarized image, all taken with the orange filter (bandpass of 540 – 640 nm) in the binned format of 512×512 pixels.

The standard preprocessing applied to the C2 raw, level 0.5 images is continuously updated to reflect the temporal evolution of the performances of C2, in particular its absolute calibration based on the photometric measurements of thousand of observations of stars present in the C2 field of view (Gardès, Lamy, and Llebaria, 2013). This procedure and the separation of the K and F coronae and of the instrumental stray light are described in Lamy *et al.* (2014) and are summarized in the Appendix. Ultimately, we obtain a set of calibrated radiance maps of the K-corona that samples the period 1996.0 to 2014.5, that is 18.5 years, thus exceeding a solar cycle and a half.

2.2. Description of Selected Solar Proxies

As evidenced from past investigations, coronal activity is linked to solar activity, and an important part of our analysis will be devoted to a comparison between the two variations. We naturally make use of different standard indices and proxies of solar activity with the purpose of identifying those that are best correlated to coronal activity and thus tracing their origins. They are briefly described below based on the works of *e.g.* Tapping (2006), Hathaway (2010), and Usoskin (2013) and are listed in Table 2.

The sunspot number (SSN) is the traditional indicator of solar activity, and we use the international sunspot number (R_i), which is determined as the weighted average of the measurements from more than 20 approved observatories. Next, the sunspot area (SSA) is thought to be a more physical measure of solar activity (Hathaway, 2010), presumably because of its more direct connection to magnetic activity. Both SSN and SSA are photospheric indices.

Another photospheric proxy is the total solar irradiance (TSI), and we rely on the data of SOHO/VIRGO, which cover the same period as the LASCO data. We benefited from the most recent daily record of VIRGO TSI filled with ACRIM-II data during the SOHO long interruption (forming the so-called PMOD composite) prepared and kindly made available to us by C. Fröhlich. The last photospheric proxy to be used in our study is the total magnetic flux (TMF) as calculated from the Wilcox Solar Observatory photospheric field maps by Y.-M. Wang and kindly made available to us; the details can be found in Wang and Sheeley (2003). The TMF is given per Carrington rotation and has been resampled on a monthly scale to match our presentation of the LASCO data.

The F10.7 index, the disk-integrated emission from the Sun at radio wavelength of 10.7 cm, represents a mixture of chromospheric and inner coronal activities. Its well-known advantage stems from being completely objective and nearly uninterrupted by weather conditions, thus forming a continuous, consistent record of activity. Finally, we consider the coronal index based on the total irradiance of the coronal green line produced by the strong emission of Fe XIV at 530.3 nm (the coronal green line) measured at five observatories, which is considered a basic optical index of solar activity (Usoskin, 2013). Unfortunately, the coronal index dataset lasts only until 2008.

With the exception of TSI and TMF mentioned above, the data were taken directly from open-access databases; see Table 2. An inter-comparison of these various proxies is

Table 2 List of selected solar indices/proxies.

Index/proxy	Origin	Source of data
Sunspot number (SSN)	Photosphere	SIDC[1]
Sunspot area (SSA)	Photosphere	RGO[2]
Total solar irradiance (TSI)	Photosphere	PMOD[3]
Total photospheric magnetic flux (TMF)	Photosphere	Y.-M. Wang
Decimetric radio flux at 10.7 cm (F10.7)	Chromosphere + corona	NOAA[4]
Coronal index (Fe XIV emission line at 530.3 nm)	Corona	NOAA[5]

[1] http://sidc.oma.be/silso/datafiles.

[2] http://solarscience.msfc.nasa.gov/greenwch.shtml.

[3] ftp://ftp.pmodwrc.ch/pub/virgo/data/IrradianceData/.

[4] http://www.ngdc.noaa.gov/stp/space-weather/solar-data/solar-features/solar-radio/.

[5] http://www.ngdc.noaa.gov/stp/space-weather/solar-data/solar-indices/.

of course not the subject of the present work; it is extensively discussed for instance by Hathaway (2010).

3. Methodology

Following the method implemented by Lamy *et al.* (2014), the radiance images of the K-corona are first globally integrated in an annular region extending from 2.7 to 5.5 $R_{\odot}$, thus slightly restricting the field of view of C2 to avoid possible traces of stray light from the occulter in the inner region and dropping the outer region of low coronal signal. Because the SOHO-Sun distance varies due to the slight eccentricity of the Earth orbit (and therefore of the L2 Lagrangian point), the size of the inner and the outer radii expressed in pixels varies accordingly to precisely measure the same region of the solar corona throughout the year. We then restrict the integral to different latitude sectors to obtain a more detailed insight of the evolution. We first consider the two hemispheres north and south separately as their solar counterparts exhibit different behaviors with a phase difference, as noted in numerous works and reflected for instance in the sunspot numbers and areas – see *e.g.* Hathaway (2010). This effect is expected to be even more pronounced in the north and south royal zones, and Bisoi *et al.* (2014), for instance, found that the hemispheric asymmetry during Solar Cycle 23 was confined to the latitude range of 45° to 60°. We broadly define the royal zones as 30° wide, extending from latitudes 35° to 65° in the northern quadrants and from −35° to −65° in the southern quadrants and combine the east and west sides to form north and south royal zones. We finally introduce three latitude sectors 30° wide centered on the equator (east and west sides combined), and on the polar north and south directions as illustrated in Figure 1. Following a change of SOHO pointing from solar to ecliptic that took place on 29 October 2010, the direction of solar north oscillates in the images; this effect is taken into account in the generation of the sectors. We calculate monthly averages of the radiance of the K-corona from these different integrals, which constitute the basic dataset of our analysis, as well as the standard 13-month running averages when a smoother view is more adequate.
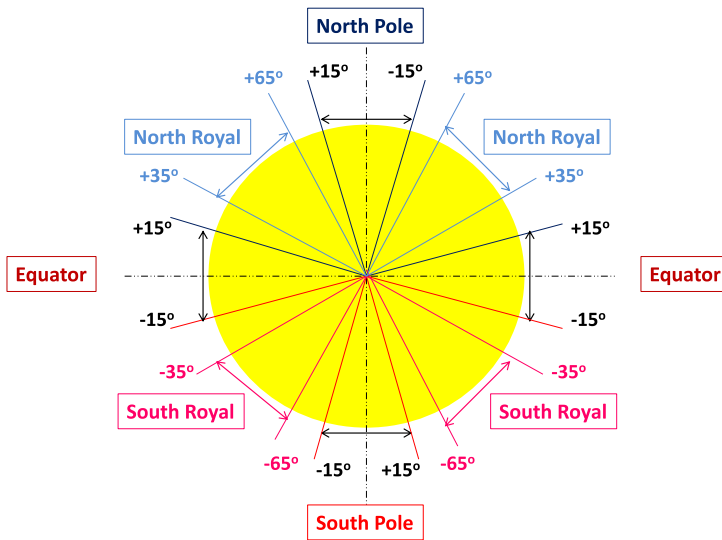
Figure 1 Schematic representation of the sectors chosen for the analysis of the K-corona radiance.

In a first approach and in line with past analysis, we broadly characterize the temporal variation of the K-corona over 18.5 years by calculating the so-called modulation factors that are defined as the ratios of the maximum and minimum of the integrated radiances. Then detailed spectral analysis and correlation analysis are performed on our different datasets (the missing data are interpolated from neighboring data to avoid discontinuities). These analyses are based on the wavelet method – see Torrence and Compo (1998) and references therein – which has been widely used in solar physics (Hathaway, 2010; Benevolenskaya and Kostuchenko, 2013; Telloni *et al.*, 2013). Being locally nonlinear, it allows tracing the evolution of stable as well as unstable signals. In this work, we use the "Morlet" wavelet as the localized wavelet function, and $\omega_0 = 6.0$ (ω_0 is a non-dimensional parameter to satisfy the admissibility condition). The result of the wavelet analysis of a given dataset is visualized as a time-frequency spectrum. The zones affected by edge effects (due to limited time intervals) are shaded and define the so-called cone of influence. Statistically significant signals (defined here as exceeding the 95 % significance level against the red noise background) are contoured by black thick lines. The noise of most real signals is not uniform (white), but correlated or red – see for instance Ostryakov and Usoskin (1990), Oliver and Ballester (1996), Frick *et al.* (1997) – and its variance depends upon the level of the signal. Likewise, we calculate wavelet cross-coherence and phase spectra, where zones of coherence between two considered datasets and the phase lag between them are simultaneously displayed; see Torrence and Compo (1998), Maraun and Kurths (2004), and Grinsted, Moore, and Jevrejeva (2004) for details. Cones of influence and statistical significance of the signals are similar to those of the wavelet analysis. In addition, time lags are visualized by arrows with the following codes: → the two datasets are in phase, ← the two datasets are in antiphase, ↓ the first dataset is leading the second one by one quarter of the period, ↑ either the first dataset is leading the second one by three quarters of the period or the second data set is leading the first one by one quarter of the period. Intermediate situations can be estimated from the more or less pronounced deviations of the arrows from the closest orientations described above.

4. Coronal Activity

4.1. Temporal Variations of the Coronal Radiance

Figure 2 presents the monthly averages of the coronal radiance, globally and in the different sectors. The long-term evolution of the global corona is characterized by the solar (Schwabe) cycle. Superimposed on this solar cycle variation, short-term oscillations are conspicuous, prominently during the maximum of Solar Cycle 23 with a period of about one year and less pronounced during the ascending and maximum phases of Solar Cycle 24 with a period of seven to eight months. The variations in the two hemispheres closely follow that of the global corona, but with subtle differences between the two: a slightly weaker Solar Cycle 22/23 minimum in the north compared to the south and, in contrast, a stronger peak in the northern hemisphere at the end of 1999. We note that the oscillations during Solar Cycle 24 are not strictly in phase, in contrast to those pervading the maximum of Solar Cycle 23. The differences are more pronounced in the two royal zones, where the northern one is conspicuously leading the southern one during the ascending branch of Solar Cycle 24 by ≈ 8 months. The two radiances then leveled off at about the same value by mid-2012. The same behavior is observed in the polar sectors; their radiance reaches about the same level only in mid-2013, roughly one year after this occurred in the royal zones. We also note the very different evolutions during the maximum of Solar Cycle 23. The northern sector experienced an abrupt increase in late 1999, but the corresponding maximum lasted slightly less than two years. In contrast, the southern sector experienced several maxima of progressively increasing amplitude that finally vanished over a time interval of approximately five years. The variation in the equatorial sector is totally at odds with the other ones and does not even follow the solar cycle. One can roughly distinguish two phases, the first one with a high mean level lasting from 1996 to 2002 (with several peaks consistent with those observed in the global corona during the maximum of Solar Cycle 23) followed by a phase of lower mean level starting with the ascending branch of Solar Cycle 24, the two mean levels being in the ratio of ≈ 1.75.

The general trends of temporal evolution described above may in part be explained by the behavior of the streamer belt, which, to a large extent, controls the radiance of the corona. During the minima of solar activity, it remains concentrated in the equatorial band, and streamers are absent at high latitudes. During the maxima, it persists in the equatorial band but also widens out to reach high-latitude regions where, in addition, pseudo and polar streamers emerge, thus contributing to the increase of the radiance observed in the two hemispheres and royal sectors.

4.2. Modulation Factor of the Coronal Radiance

Figure 2 illustrates the difficulty of defining a meaningful modulation factor and even questions the value of such a factor, especially when comparing results of eclipses obtained during solar maxima if oscillations such as those observed during Solar Cycle 23 are present. The occurrence of an anomalously deep minimum (23/24) presents another difficulty, leading to the introduction of two modulation factors MF_1 and MF_2 that are defined as the ratios between the maximum radiance recorded during Solar Cycle 23 and the 22/23 and 23/24 minima, respectively. We also introduce MF_3 as the ratio of the present maximum of Solar Cycle 24 to the 23/24 minimum. Table 3 displays these three modulation factors calculated from 13-month running averages as more representative of the long-term variations.
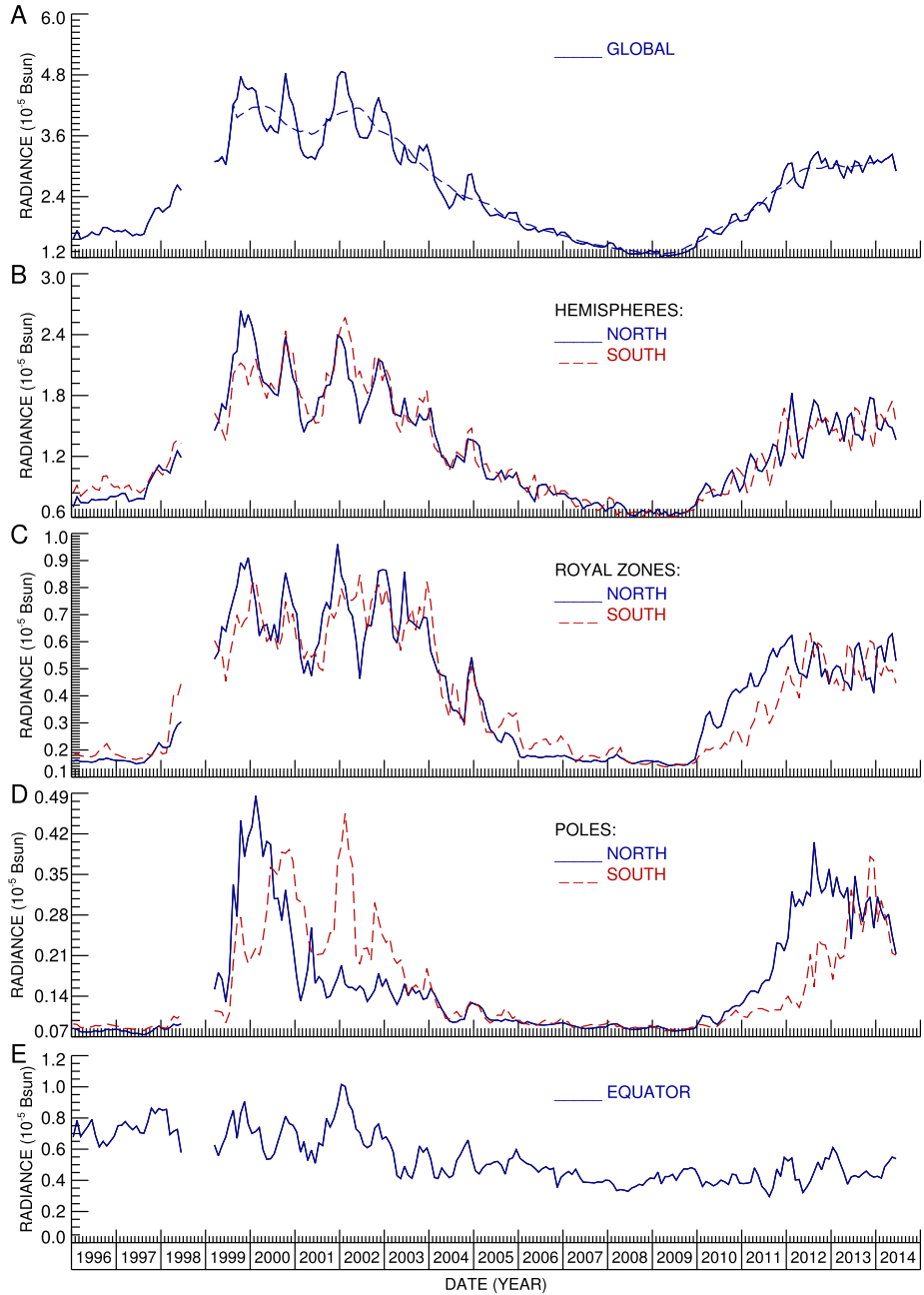
Figure 2 Monthly averaged temporal variations of the radiance of the K-corona integrated from 2.7 to 5.5 $R_{\odot}$ globally and in different sectors: (A) global corona (the dashed line corresponds to the 13-month running average), (B) northern and southern hemispheres, (C) northern and southern royal sectors, (D) north and south polar sectors, and (E) equatorial sector. We note the different scales of the radiance (vertical) axes.

Table 3 Modulation factors of the radiance of the K-corona MF_1, MF_2, and MF_3 as defined in the text and calculated from the 13-month running averages of the radiance data.

Solar sector	MF_1	MF_2	MF_3
Global	2.7	3.3	2.5
Northern hemisphere	3.1	3.4	2.5
Southern hemisphere	2.7	3.5	2.8
Northern royal	4.8	5.0	4.2
Southern royal	4.4	5.3	3.6
North pole	4.9	4.6	4.0
South pole	3.9	3.9	3.6
Equator	1.2	2.2	1.5

These factors amount to $MF_1 = 2.7$, $MF_2 = 3.3$, and $MF_3 = 2.5$ for the global corona using the smoothed dataset, but reach $MF_1 = 3.1$, $MF_2 = 4.0$, and $MF_3 = 2.7$ for the original dataset. They are systematically larger than the bulk of past results (Table 1), but are still in line with that of Lebecq, Koutchmy, and Stellemacher (1985). Considering the modulation factors in different sectors, the strongest variations are observed in the royal zones, closely followed by the polar regions and then the two hemispheres, whereas the weakest are found in the equatorial band.

4.3. Analysis of the Short-Term Variations

As already pointed out, the radiance of the global K-corona and that in several sectors exhibits prominent oscillations during the maximum of Solar Cycle 23 with a period of about one year (Figure 2). There are several indisputable arguments against attributing its origin to instrumental stray light from the Sun. First, the amplitude of the oscillation of up to 60 % would require a huge amplification effect compared to the geometric variation resulting from the variation of the Sun-SOHO distance (3.4 %). Second, stray-light oscillations would be even more conspicuous during the minimum of Solar Cycle 23/24 when the K-corona radiance itself reaches minimum. Third, oscillations are also present during the ascending phase of Solar Cycle 24, but at a different, reduced period (seven to eight months). We now analyze these short-term variations in detail in the framework of the wavelet method.

4.3.1. Wavelet Analysis of the Coronal Radiance

Figure 3 displays the wavelet spectra of the coronal radiance globally and in the different sectors. The most stable and statistically significant maxima of the wavelet amplitude are seen at the quasi-annual period in all cases except the polar sectors and at a slightly reduced level in the south royal zone. The contours at 95 % significance level in the time-frequency spectra extend over six years (1999 to 2004 inclusive) corresponding to the maximum phase of Solar Cycle 23 and to periods ranging from roughly 9 to 14 months. No statistically significant oscillations are detected thereafter during the 23/24 minimum. Secondary, much less intense maxima are then seen starting in 2010 with the ascending phase of Solar Cycle 24, most prominently in the equatorial sector and the northern and southern hemispheres; their periods broadly extend from six to nine months. We note a possible resumption of the period of about one year in late 2011 in the equatorial sector, but it presently is at the limit of the cone of influence. The polar sectors are clearly at odds with the above behavior. The south polar sector exhibits a statistically significant maximum lasting about two years centered at the solar maximum with periods centered at 16 months with a short extension to about
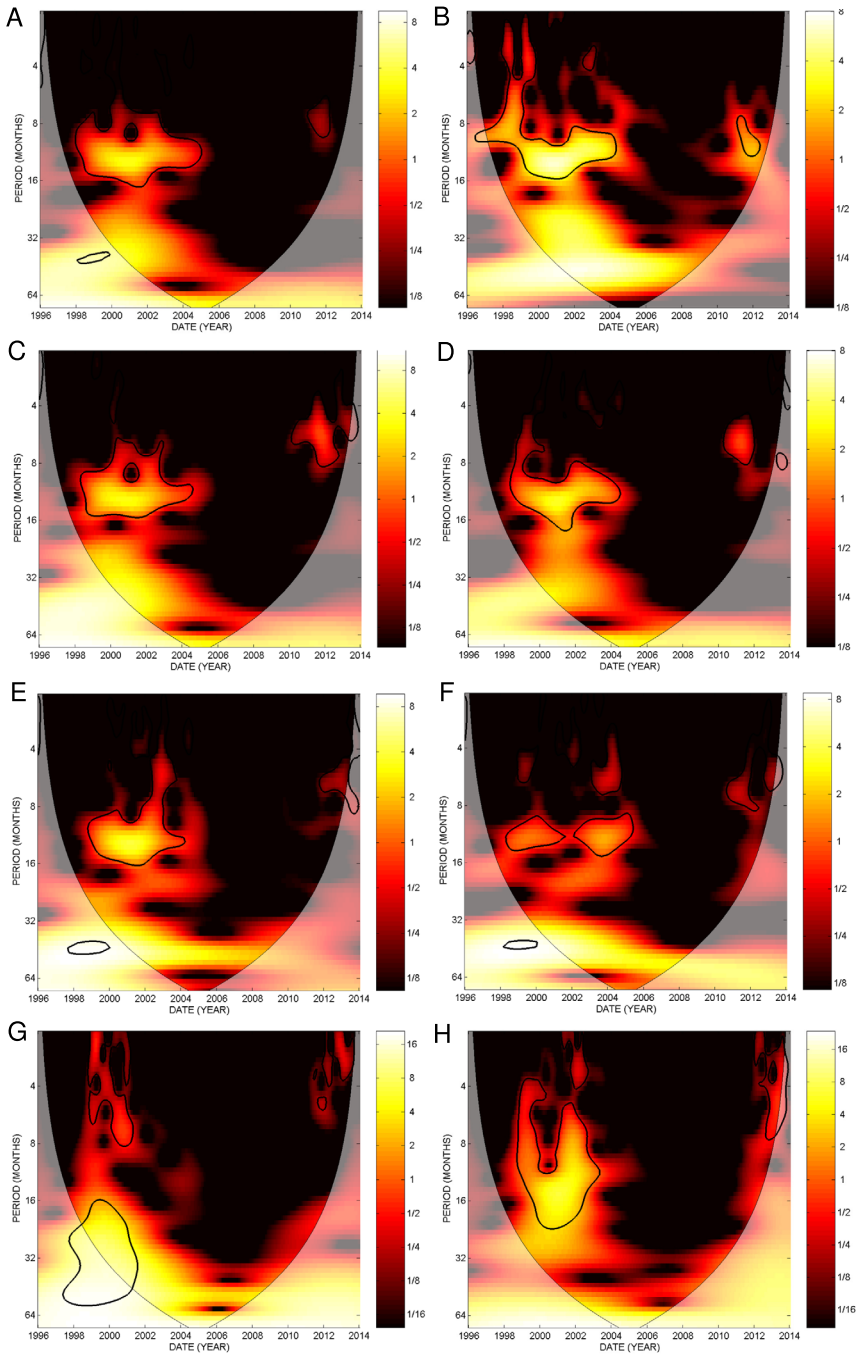
Figure 3 Wavelet spectra of the K-corona radiance: global corona (A), equatorial sector (B), northern and southern hemispheres (C and D), northern and southern royal zones (E and F), and north and south polar sectors (G and H). The color bars provide the scales for the wavelet power amplitude.
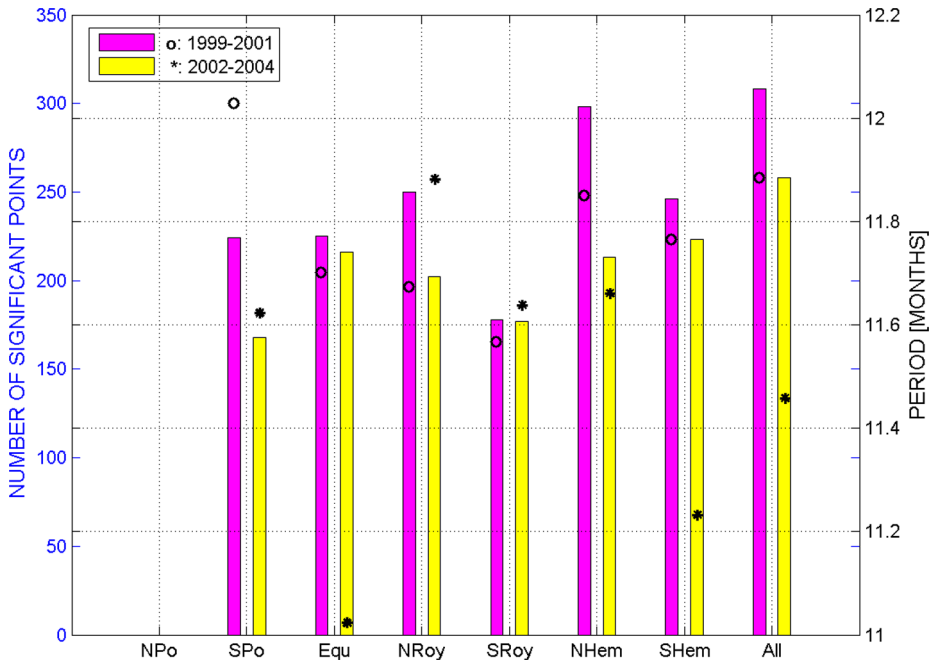
Figure 4 Analysis of the period shifts in two time intervals of Solar Cycle 23, 1999–2001 and 2002–2004. The vertical bars represent the number of significant points used to calculate the mean periods (left axis). The symbols correspond to the mean periods (right axis). The maximum phase in the north polar sector was too short to develop an oscillation pattern.

12 months at the beginning of 2002. As evident in Figure 2, the maximum phase in the north polar sector was just too short, lasting about two years, to develop an oscillation pattern.

Closer examination of Figure 3 indicates that several contours relevant to the quasi-annual oscillation suggest two different regimes with slightly different periods between the first three years of the solar maximum (1999–2001) and the following three years (2002–2004), prominently in the equatorial sector and in the southern hemisphere. We investigated this question by calculating the mean of the periods at maximum wavelet amplitude separately in each of the above two time intervals. Figure 4 displays two kinds of information. First, the vertical bars represent the numbers of statistically significant points used in the calculation. They range from ≈ 170 to ≈ 310, which ensures the validity of the analysis. Second, the symbols indicate the periods. As suspected from the wavelet spectra, the largest shifts are observed in the equatorial sector (from 11.7 to 11.0 months) and in the southern hemisphere (from 11.8 to 11.2 months). Shorter decreases are found for the global corona and the south polar sector (typically 0.4 month) and the northern hemisphere (0.2 month). In contrast, the royal zones witnessed a modest increase of their periods between the two time intervals, almost negligible for the southern one and of about 0.2 month for the zone in the north. We did not attempt to perform this type of analysis for (incomplete) Solar Cycle 24 as the relevant regions of the wavelet spectra are presently affected by the cones of influence. At the moment, we therefore cannot conclude whether the above shifts are a specific feature of Solar Cycle 23 or if they may be present in different solar cycles.
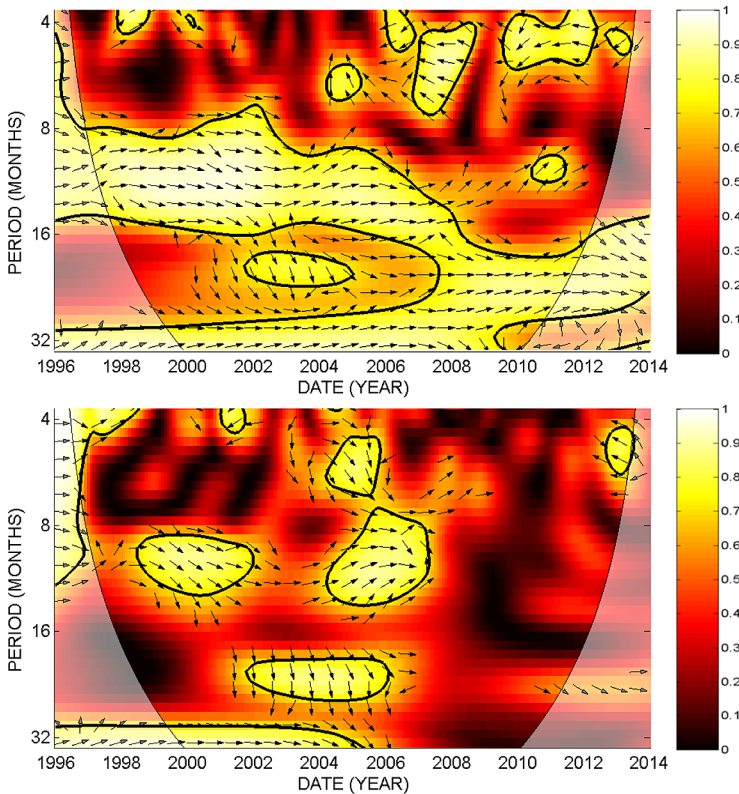
Figure 5 Wavelet cross-coherence and phase spectra of the radiance of the K-corona in the northern and southern hemispheres (upper panel) and in the northern and southern royal zones (lower panel). The color bars provide the scale for the wavelet power amplitude.

4.3.2. *Wavelet Cross Coherence and Phase Analysis of the North–South Asymmetry*

In Section 4.1, we have already pointed out the north-south asymmetry in the temporal evolution of the coronal radiance. We further analyze this asymmetry in the case of the short-term variations by presenting the wavelet cross-coherence and phase spectra of the radiance of the two hemispheres and of the two royal zones (Figure 5).

The first spectrum (upper panel) exhibits a statistically significant and highly stable band of coherence with oscillations at periods ranging from 9 to 14 months during the whole Solar Cycle 23 and progressively shifting to higher periods ($\approx 17-30$ months, *i.e.* about twice the above range). The two hemispheres are mostly in phase, but there are short intervals of alternative leadings; however, the longest time lag does not exceed two months. During the minimum of activity, there are some very short intervals of coherence at periods between four and eight months and a three-year interval of coherence at periods between four and five months during the ascending branch of Solar Cycle 24, the two hemispheres being roughly in antiphase in these cases.

The second spectrum relevant to the royal zones (lower panel of Figure 5) shares some similarity with that of the hemispheres during Solar Cycle 23 but with less stability; it exhibits several notable differences, however. For instance, the coherence with periods between 9 and 14 months observed as a stable band in the case of the hemispheres is separated into

Table 4 Correlation coefficients *R* between the radiance of the K-corona and the selected proxies using 13-month running averages. The results are given for the 18.5-year time span covering Solar Cycles 23 and partly 24, and separately for Solar Cycle 23 and part of Solar Cycle 24.

Proxy	*R*		
	23 – 24	23	24
TMF	0.98	0.99	0.98
TSI	0.97	0.98	0.96
F10.7	0.97	0.97	0.95
SSA	0.96	0.97	0.91
Fe XIV	–	0.96	–
SSN	0.92	0.92	0.85

two "islands" two to three years long. In these two islands, the two royal zones are roughly in phase, but less coherently so than the two hemispheres because short time lags are present. Finally, we note that there is one island of coherence with periods of about five to seven months during the interval 2004 – 2006 and none thereafter (until 2013), in contrast to the case of the hemispheres.

In conclusion, the hemispheres, which naturally cover broad regions of the corona, tend to exhibit a clearer pattern than the more localized royal zones, which may be subjected to different patterns of activity. In both cases, hemispheres and royal zones, a stable significant coherence at about a two-year period is present during the 2002 – 2006 time interval, perhaps a harmonic of the period of about one year, although in the former case, the northern sectors are clearly leading the southern ones.

5. Comparison of Coronal and Solar Activities

In this section, we compare the temporal variations of the coronal radiance, globally and in different solar sectors, with those of the solar proxies introduced in Section 2.2. As in the case of coronal activity, we first consider the solar cycle variations and then the short-term oscillations.

5.1. Solar Cycle Variations

Using 13-month running averages appropriate to long-term variations, we calculated the correlation coefficients between the global K-corona radiance and the different proxies (Table 4). The coefficients are quite large, ranging from 0.99 to 0.96 for TMF, TSI, F10.7, SSA, and Fe XIV, and slightly smaller for SSN (0.92). In this table, we also separate the two solar cycles: the full Solar Cycle 23 extending from 1996.0 to 2009.0 and the partial Solar Cycle 24 thereafter until 2014.5 (with the exception of the Fe XIV coronal index, for which data are only available during Solar Cycle 23). While the coefficients remain large for the former cycle, even slightly exceeding those obtained over the full 18.5-year interval, they tend to be slightly smaller for the latter cycle, for instance only 0.85 for SSN. This suggests less pronounced correlations between the coronal radiance and the proxies during the ascending and maximum phases of Solar Cycle 24.

Figure 6 summarizes the results for the correlation coefficients. There is a trend of the correlations to slightly decrease as the sectors become more restricted, notably from global to hemispheres, to royal zones, to the equatorial band and to the south polar sector. Consistent with the anomalous temporal variations exhibited by the north polar sector (Figure 2),
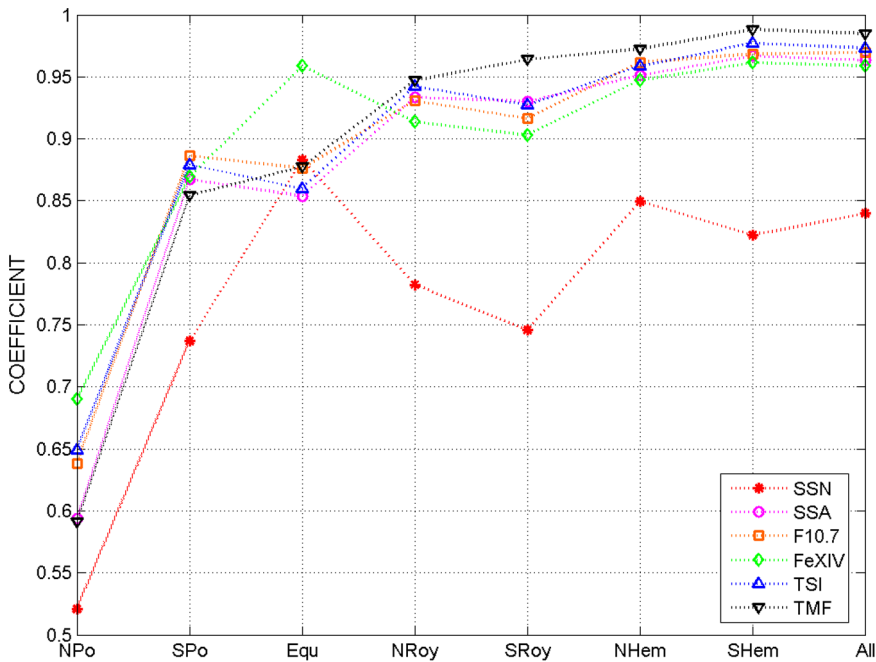
Figure 6 Correlation coefficients between the radiance of the K-corona globally (denoted "All") and different sectors and the selected proxies using 13-month running averages.

Table 5 Duration of Solar Cycle 23 and modulation factors MF_1, MF_2, and MF_3 as defined in the text for the coronal radiance and the solar proxies using 13-month running averages.

Proxy	Cycle duration Year & Month ± 2	MF_1	MF_2	MF_3
Corona	12 & 3	2.7	3.3	2.5
TMF	12 & 3	4.0	7.6	4.8
TSI	12 & 3	1.001	1.001	1.001
SSA	12 & 3	–	–	–
Fe XIV	12 & 4	5.7	8.6	–
F10.7	12 & 5	2.7	2.9	2.4
SSN	12 & 6	–	–	–

the corresponding radiance–proxies correlation coefficients are conspicuously lower than in the other sectors.

In the set of graphs displaying the temporal variations of the coronal radiance with the different proxies, their scales were chosen so that the curves closely match for an easy comparison. However, this tends to incorrectly suggest that the variations have the same amplitude, which is obviously not the case. To properly assess the real amplitudes, we calculated three modulation factors MF_1, MF_2, and MF_3 as defined in Section 4.2 for the proxies – with the exception of SSN and SSA, which reach the zero value during the minimum between Solar Cycles 23/24 – using 13-month running averages (Table 5). The proxy with the modulation factors closest to those of the global radiance is the F10.7 radio flux, which can be understood as they are both connected to the corona, at least in part for F10.7. The

Fe XIV coronal index expresses the variation of the emission of the green line prominently within 2 $R_\odot$ and is known to vanish more strongly than the white-light outer corona during solar minima, hence the larger modulation factors. In addition, the activity patterns of the green-line and white-light coronae may be significantly different, as illustrated by the maps at 1.15 $R_\odot$ for the former and 3.0 $R_\odot$ for the latter of Tappin and Altrock (2013); see their Figure 2. TMF and TSI are not directly quantitatively linked to the coronal radiance, hence their very different modulation factors especially for TSI.

We finally consider the question of the duration of the Schwabe cycle of the K-corona radiance compared to those of the different proxies. As extensively discussed by Hathaway (2010), the determination of the dates of the solar minima (and maxima as well) is extremely tricky and depends upon the (noisy) data, their smoothing, and the chosen criteria. Because the LASCO observations of the 22/23 minimum are incomplete, Lamy *et al.* (2014) used the phasing of the successive ascending branches of Solar Cycles 23 and 24 to determine a cyclic period of 12 years and 3 months for the coronal radiance. We applied the same procedure to the solar proxies so as to establish a sound comparison based on the same criterion and present our results in Table 5, emphasizing that the uncertainty of this method is typically ± 2 months. We note that i) the dates of the minima of the TSI reported by Fröhlich (2013) yield a duration of 12 years and 3 months, and that ii) Hathaway (2010) found 12 years and 7 months using the minima of the 13-month mean of the international sunspot number, but only 12 years and 3 months when taking the average of three determinations (see his Table 2). Therefore we do not consider that the differences in duration displayed in Table 5 reflect any profound physical process and that they simply altogether concur in the well-recognized anomalously (yet not exceptionally) long Solar Cycle 23.

5.2. Short-Term Variations

In the same way as for the K-corona radiance, all selected proxies exhibit significant short-term variations at a variety of periods; see Figure 7 and the upper panels of Figures 8, 9, and 10. Visual inspection of these curves allows a first comparison between the behavior of the coronal radiance and those of the proxies. Both SSN and SSA exhibit pronounced oscillations at periods shorter than one year, which are absent in the coronal radiance but also in the other proxies. Surprisingly, the Fe XIV coronal index and the coronal radiance share only a few temporal features, but overall the patterns of variation are quite dissimilar. The similarity clearly improves with the radio flux and is even stronger with the TSI and TMF proxies. These visual results are quantitatively confirmed by the wavelet cross-coherence and phase spectra. They are only displayed in the case of the last three proxies, F10.7, TSI, and TMF (see the lower panels of Figures 8, 9, and 10) because those relevant to the other proxies do not contain any significant information.

The spectrum of coronal radiance – F10.7 shows three regimes of coherence: a first one at a period of about two years extending over the ascending branch and maximum of Solar Cycle 23, a second one quite broad (width of about eight months) centered at one year and extending over the second part of the maximum of Solar Cycle 23 and its descending branch, and the third one at a period of seven to eight months extending over the ascending branch and maximum of Solar Cycle 24. In the first two cases, the variations are separated by either one quarter or three quarters of a period, whereas they are in antiphase in the third case.

The spectra of coronal radiance – TSI and coronal radiance – TMF show nearly the same pattern with two pronounced zones of coherence, a first one at a period of about one year extending over most of Solar Cycle 23, and a second one at a period of seven to eight months extending over the ascending branch of Solar Cycle 24. In the first spectrum, the variations
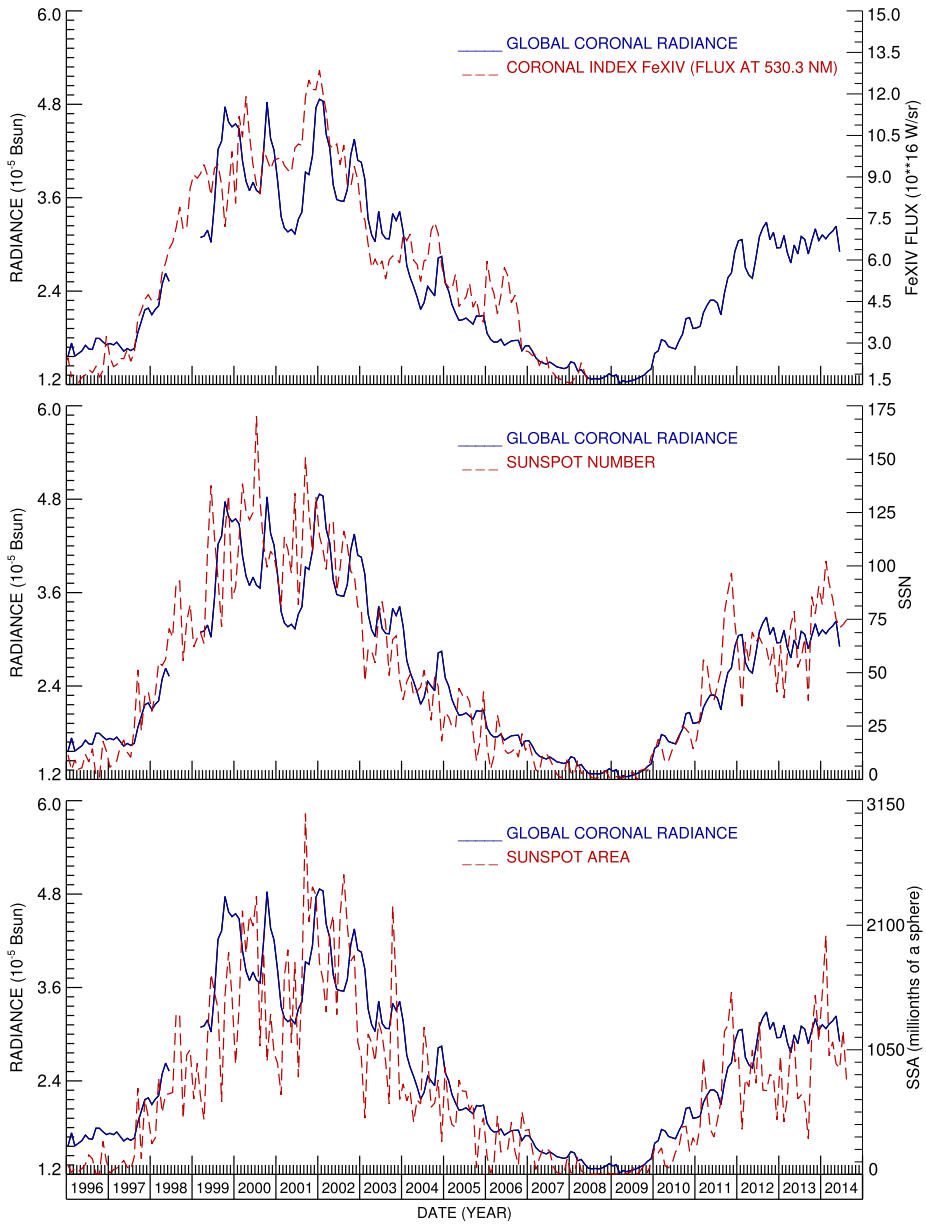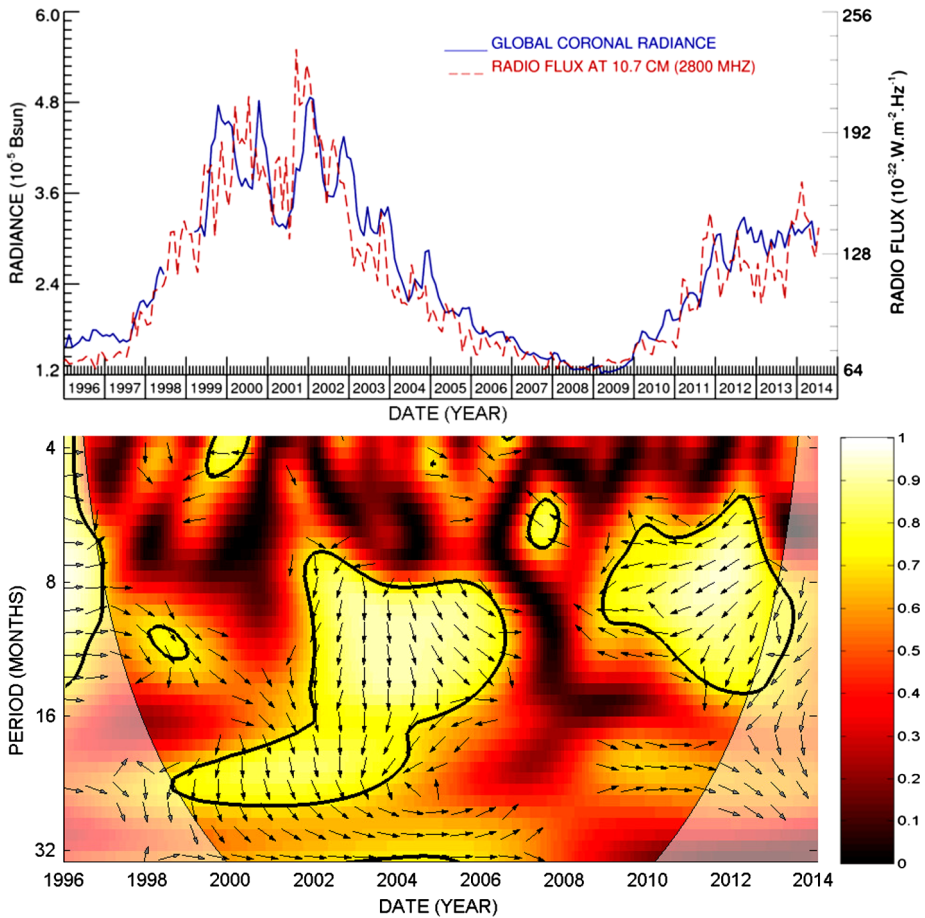
Figure 7 Temporal variations of the radiance of the K-corona integrated from 2.7 to 5.5 $R_\odot$ and of the Fe XIV coronal index (upper panel), SSN (middle panel), and SSA (lower panel) proxies. All data are monthly averages.

are in antiphase or close to it (second coherence zone). In the second spectrum, the phase lag in the first coherence zone is poorly defined, while the variations are clearly in antiphase in the second zone. Therefore the patterns of phase lag between the TSI and TMF indices themselves are not entirely consistent.

Figure 8 Temporal variations of the radiance of the K-corona integrated from 2.7 to 5.5 $R_\odot$ and of the F10.7 radio flux (upper panel) and their wavelet cross-coherence and phase spectrum (lower panel).

6. Discussion

Our results based on the analysis of the integrated radiance of the K-corona from 2.7 to 5.5 $R_\odot$ clearly show that the solar cycle can be traced high into the solar corona – and even beyond 5.5 $R_\odot$ based on the work of Tappin and Altrock (2013) – and furthermore allows delineating spatially resolved patterns of activity. The correlations and cross-correlations with several proxies of solar activity are extremely strong, with correlation coefficients ≥ 0.96 for most of them. The highest correlation is found with the TMF proxy, followed by TSI, F10.7, SSA, and the Fe XIV coronal index, and the lowest with SSN. The modulation factors, which are the amplitudes of the variation between successive solar maxima and minima, very much depend upon the strength of the cycle and also on how the data are averaged. Using 13-month running averages, the coronal radiance exhibits modulation factors of 2.7, 3.3, and 2.5 starting from the Solar Cycle 22/23 minimum to the maximum of Solar Cycle 24, rather comparable to those of the F10.7 radio flux, but significantly lower than the other proxies. The modulation factors furthermore strongly depend upon the heliographic
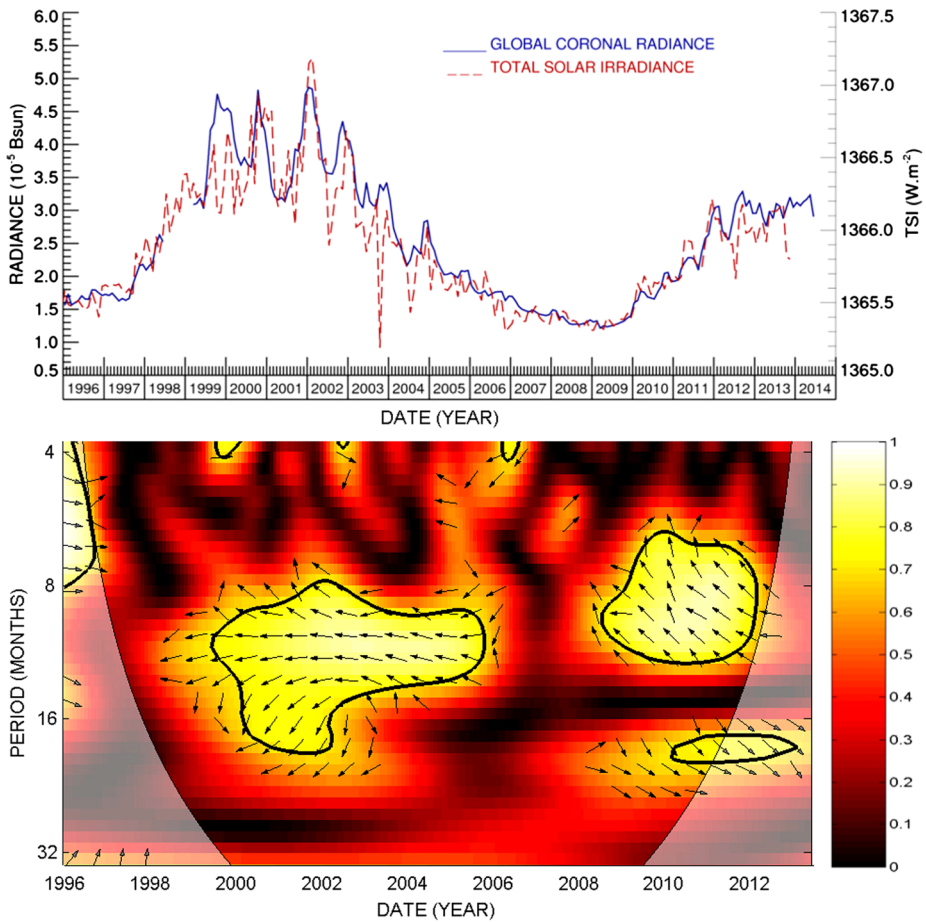
Figure 9 Temporal variations of the radiance of the K-corona integrated from 2.7 to 5.5 $R_\odot$ and of the TSI proxy (upper panel) and their wavelet cross-coherence and phase spectrum (lower panel).

latitude, being the largest in the royal and polar sectors and the smallest in the equatorial band where the solar cycle pattern is barely present. A slight asymmetry is present between the temporal variations of the K-corona radiance of the northern and southern hemispheres, with the former one leading the second one by one month. A similar behavior is observed in the royal sectors with a larger time lag between the two ascending branches, here again the northern one leading the southern one by about eight months. A more complex evolution is found for the two polar sectors with totally different behaviors during the maximum of Solar Cycle 23 and during the ascending branch of Solar Cycle 24, where the lag between the leading northern sector and the southern sector exceeds one year. Consequently, the two sectors reached their maxima at very different dates, about 2012.0 for the northern one and about 2013.5 for the southern one. This is fully consistent with numerous works, *e.g.* Petrie (2012), Gopalswamy *et al.* (2012), Altrock (2013), McIntosh *et al.* (2013), which all point to the phase lag of the onset of Solar Cycle 24 activity between the two polar regions. Using the *Solar Dynamics Observatory* images obtained during the ascending phase of Solar Cycle 24, Benevolenskaya, Slater, and Lemen (2014) found a north-south asymmetry of the
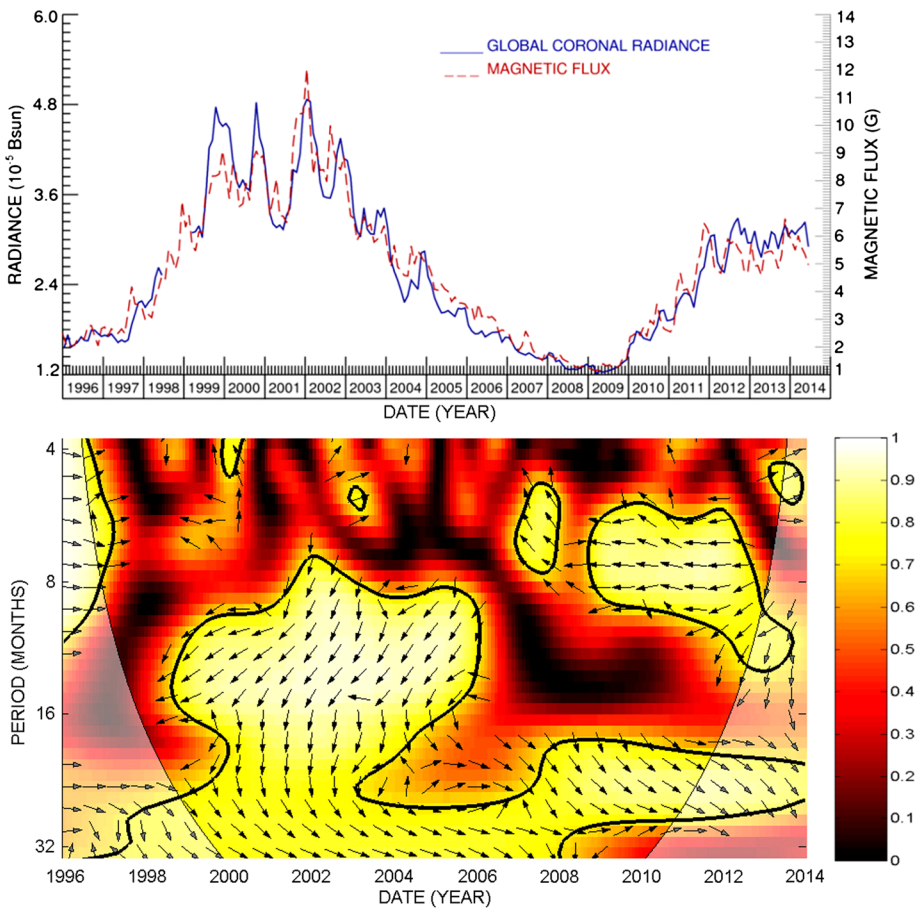
Figure 10 Temporal variations of the radiance of the K-corona integrated from 2.7 to 5.5 $R_{\odot}$ and of the TMF proxy (upper panel) and their wavelet cross-coherence and phase spectrum (lower panel).

EUV intensity and of the emerging magnetic field at high-latitudes that resulted in an asymmetry in the timing of the polar magnetic field reversals. The unequal distribution of various manifestations of solar activity between the northern and southern hemispheres of the Sun has been known for over a century (*e.g.* Bisoi *et al.*, 2014) and has later been detected in the interplanetary medium (solar wind and interplanetary magnetic field) and geomagnetic index – see *e.g.* Nair and Nayar (2008). It is part of a more general evolution of solar magnetic activity that is due to the solar dynamo (Krivodubskij, 2005). The hemispheric phase difference appears to belong to a broad secular variation with reversals occurring roughly every eight solar cycles. The last one took place in 1968 and saw the northern hemisphere taking over the southern one (Zolotova *et al.*, 2010). However, the large time lag exceeding one year between the Solar Cycle 24 maxima observed in the royal and polar sectors is probably linked to the anomalously long minimum of Solar Cycle 23/24. The increase of the latitudinal extension of the Sun's meridional flow all the way to the poles during Solar Cycle 23 (Dikpati *et al.*, 2010; Dikpati, 2011) has been advocated as the cause of this long and deep 23/24 minimum, which additionally weakens the polar fields (Wang, Robbrecht, and Sheeley, 2009). This is probably also related to the observed (from helioseismic data) dif-

ferent behavior of solar oscillation frequencies in the subsurface magnetic layers during the descending branch of Solar Cycle 23 compared to that of Solar Cycle 22 (Basu *et al.*, 2012), which indicates changes in the underlying solar dynamo processes such as the meridional flow rates and the magnetic-flux emergence.

Most interesting and intriguing are the oscillations at periods of about one year over most of Solar Cycle 23 and of about seven to eight months over the ascending and maximum phases of Solar Cycle 24 (Figure 3). These quasi-periodic variations are in fact not stable, and the first regime ranges from 11.2 to 12 months depending upon sectors and additional changes by one to two months between the first and second parts of Solar Cycle 23 (Figure 4). Multiple periodicities have been found in essentially all physical features and quantities that reflect solar activity extending from the 27-day synodic rotation to the approximately 11 years of the Schwabe solar cycle. Best examples are i) the 154-day periodicity discovered by Rieger *et al.* (1984) in the temporal distribution of flares that was subsequently found in a variety of solar data: SSN, SSA, F10.7, sunspot-blocking function – see for instance the works of Lean and Brueckner (1989), Lean (1990), Oliver, Ballester, and Baudin (1998), and ii) the 1.3-year periodicity detected using helioseismology at the base of the solar convection zone (Howe *et al.*, 2000, 2007) and in SSA and SSN time series (Krivova and Solanki, 2002). These multiple periodicities collectively known as intermediate or mid-term quasi-periodicities together with those in the range of $0.6 - 4$ years are often referred to as quasi-biennial oscillations (QBOs) in the literature. They are the subject of a recent in-depth review by Bazilevskaya *et al.* (2014) on which we directly rely for their overall characterization as summarized below. Key features of QBOs include i) variable periodicity and intermittence, ii) presence at all levels of the solar atmosphere and even in the convective zone, iii) asymmetric, independent development in the northern and southern solar hemispheres, and finally iv) largest amplitudes during the maximum phase of solar cycles. As typical examples of these properties, Lean and Brueckner (1989) found periodicities in SSA time-series episodically appearing during the maximum phases of cycles shifting between 130 and 185 days, and Bisoi *et al.* (2014) found a hemispheric asymmetry in the periodicities of the photospheric fields analyzed over the years 1975 to 2010. It is quite remarkable that all these features are also found in the short-term variations of the radiance of the K-corona as revealed by our analysis. Therefore, the conclusions of Bazilevskaya *et al.* (2014) may be extended to the corona at large, thus bridging the transition of solar QBOs to interplanetary space.

Of the forest of mid-term quasi-periodicities ranging from 27 days to four years reported so far, only some appear to be present in the corona during the 18.5-year time interval considered in the present study; moreover, the most prominent solar QBOs with periodicities of 154 days and 1.3 year are absent. However, a one-year periodicity has been reported for several manifestations of solar activity, for instance in:

- the solar total and open fluxes (Mendoza, Velasco, and Valdés-Galicia, 2006),
- the high-latitude photospheric fields (see Figure 2 of Bisoi *et al.* (2014) and note that this periodicity is even slightly shorter than one year in the southern hemisphere),
- the rotation near the base of the convective zone (see Figure 3 of Howe *et al.* (2007) and the presence of a significant peak at ≈ 11.5 months – very close to what we found – in their spectrum during Solar Cycle 23).

Regarding our second regime of periodicities of seven to eight months ($0.56 - 0.66$ year) detected during the presently available part of Solar Cycle 24, we note that it is generally absent in solar activity, but that Kilcik *et al.* (2014) recently found periods of 213 and 248 days (*i.e.* 0.58 and 0.68 year) in their analysis of sunspot count periodicities since 1986, with the

second one conspicuously present in the *medium* groups of sunspots during the ascending branch of Solar Cycle 24.

The nature of QBOs is far from understood, and an extended discussion of their possible origins is beyond the scope of this article. We mention that the majority of researchers in this field believe that QBOs are mostly related to the dynamics of the deep layers of the Sun (Rieger *et al.*, 1984) and intrinsic to the solar dynamo mechanism, the question often translating into the possible existence of two dynamos, one at the base of the convection zone and another near the bottom of the layer extending $\approx 35\,000$ km below the solar surface. Prominent periods are thought to be generated by stochastic processes caused by the periodic emergence of magnetic flux as the solar cycle progresses, as proposed by Wang and Sheeley (2003), who also pointed out that there is no reason for a pattern of stable and reproducible periods. Benevolenskaya, Slater, and Lemen (2003) viewed the periodicities of 1.5 to 2.5 years as impulses of solar activity formed by reappearing long-lived complexes of activity, and she proposed that these impulses could be linked to the high-frequency component of the toroidal magnetic field in the double magnetic cycle model (Benevolenskaya, 1998).

As an alternative explanation, the possible role of waves has been mentioned in the literature: rotational waves due to solar *g*-modes (Wolff, 1983), solar Rossby and mixed Rossby–Poincaré hydrodynamic waves (Sturrock *et al.*, 1999; Lou, 2000; Chowdhury and Dwivedi, 2011; Chowdhury, 2011).

The extremely strong correlations of the coronal radiance – and consequently the coronal electron density – with the total magnetic flux (TMF) as demonstrated in Table 4 and Figure 10 clearly prove that the coronal activity is intimately connected to the solar magnetic field. This has been known based on the evolution of the morphology of the corona with the solar cycle but has never been quantitatively established before as we did here over an interval exceeding a solar cycle and a half and at the temporal resolution allowed by the LASCO-C2 data. The concomitant high correlations with the total irradiance (TSI) are not surprising and a consequence of the direct link between the photospheric radiance on the solar magnetic field through changes in the solar surface temperature (Tapping *et al.*, 2007); the TSI can be reconstructed based on the thermal structure of magnetic features (Krivova *et al.*, 2003) or based on surface magnetic flux changes as in the SATIRE-S model (Ball *et al.*, 2012). Although slightly less correlated, the F10.7 radio flux appears to give a good estimate of the amplitude of the solar cycle variation of the coronal radiance.

7. Conclusion

Our analysis of the radiance of the K-corona extracted from calibrated LASCO-C2 images over 18.5 years (1996.0 – 2014.5) that were integrated in an annulus extending from 2.7 to 5.5 $R_\odot$ globally and in different latitudinal sectors allowed an unprecedented quantitative characterization of its variability and, in turn, of that of the electron density. Our analysis also showed that the white-light corona contains significant spatially resolved information in regions inaccessible to *in situ* measurements (*e.g.* polar regions), giving a detailed insight on how the corona reacts to the solar activity. Our main conclusions from this study are summarized below:

1. The temporal variation of the global radiance and in turn of the total electron content of the K-corona follow the solar cycle very well, as reflected by the standard proxies of solar activity.

2. The modulation factors, which are the amplitudes of the variation between successive solar maxima and minima, very much depend on the strength of the cycle and also on how the data are averaged. Using 13-month running averages, we found successive modulation factors of 2.7, 3.3, and 2.5 starting from the minimum of Solar Cycle 22/23 to the maximum of Solar Cycle 24.

3. The modulation factors also strongly depend upon the heliographic latitude, being largest in the royal and polar sectors and smallest in the equatorial band where the solar cycle pattern is barely present.

4. An asymmetry is prominently observed in the royal sectors during the ascending phase of Solar Cycle 24, the northern leading the southern sector by approximately nine months.

5. This asymmetry is even more pronounced in the polar sectors and is already conspicuous during most of Solar Cycle 23. Consequently, the north and south polar sectors reached their maxima at very different times, ≈ 2012.0 for the former and ≈ 2013.5 for the latter.

6. Mid-term quasi-periodicities or quasi-biennial oscillations (QBOs) are present in the temporal variation of the coronal radiance, following different patterns in different latitudinal sectors. Most prominent are a quasi-annual period during the maximum of Solar Cycle 23 and a shorter period, seven to eight months, in the ascending branch and maximum of Solar Cycle 24.

7. These coronal QBOs share the same properties as the solar QBOs: variable periodicity, intermittency, asymmetric development in the northern and southern solar hemispheres, and largest amplitudes during the maximum phase of solar cycles.

8. The strongest correlations of the temporal variations of the coronal radiance – and consequently of the coronal electron density – are found with the total magnetic flux and with the total solar irradiance (which is itself known to be closely linked to the solar magnetic field). Considering that the morphology of the solar corona is also directly controlled by the topology of the magnetic field, these correlations reinforce the view that they are intimately connected, including their variability at all timescales.

9. Although slightly less correlated, the F10.7 radio flux appears to give a good estimate of the amplitude of the solar cycle variation of the coronal radiance.

Appendix: LASCO-C2 Data Preprocessing

The routine observational program is basically composed of unpolarized white-light images of 1024×1024 pixels every 20 min and a daily polarization sequence all taken with an orange filter (bandpass of $540 - 640$ nm); in addition, there have been specific campaigns usually coordinated with other SOHO instruments.

The present analysis makes use of these polarization sequences since their temporal cadence is sufficient for our purpose and since they allow extracting the K-corona following

a classical procedure to be described below. A polarization sequence is composed of three linear polarized images of the corona obtained with three polarizers oriented at 60°, 0°, and −60° and an unpolarized image, all taken with the orange filter in the binned format of 512 × 512 pixels.

All LASCO images, either polarized or unpolarized, undergo a standard preprocessing that corrects for instrumental effects. The in-flight performances of C2 are continuously monitored so as to update these corrections and the absolute calibration. Our analysis also benefits from recent improvements introduced in the procedures. The preprocessing performs the following tasks:

1. Bias correction. The bias level of the CCD detector evolves with time; it is continuously monitored using specific blind zones, and is systematically subtracted from the images.
2. Exposure-time equalization. Small random errors in the exposure times are corrected using a method developed by Llebaria and Thernisien (2001) and refined by Llebaria, Loirat, and Lamy (2010) in which relative and absolute correction factors are determined.
3. Missing-block correction. Telemetry losses result in blocks of 32 × 32 pixels sometime missing in the images. Different solutions are implemented to restore the missing signal depending upon the location of these blocks (Pagot *et al.*, 2013).
4. Cosmic-ray correction. The impact of cosmic rays (and stars) is eliminated from the images using the procedure of opening by morphological reconstruction developed by Pagot *et al.* (2013).

The polarized images also undergo the following processes:

1. Correction for the global transmission of the polarizers.
2. Correction for the spatial variation of the transmission of the polarizers (Llebaria and Lamy, 2008).
3. Correction for the circular polarization introduced by the two folding mirrors.
4. Polarimetric analysis based on the Mueller procedure. This is applied to each triplet of polarized images and returns images of the total radiance, the polarization, and the angle of polarization.
5. Vignetting correction. This instrumental effect is removed from the radiance images using a geometric model of the two-dimensional vignetting function of C2 (Llebaria, Lamy, and Bout, 2004).
6. Absolute calibration of the total radiance derived from the photometric measurements of thousands of observations of stars present in the C2 field of view (Llebaria, Lamy, and Danjard, 2006; Gardès, Lamy, and Llebaria, 2013).

At this stage, the images represent the sum of the radiances of the K and F coronae and of the instrumental stray light. The separation of the K component is performed on the basis of the classical assumptions that the F corona and the stray light are unpolarized based upon the fact that both mostly result from diffraction effects. This is indeed a valid assumption for the F corona inside 6.5 $R_\odot$. Using these assumptions, the polarized radiance pB is equal to $p_K B_K$. At this point, we use a model of p_K calculated for a standard spherical corona (Allen, 1973), which is justified by the robust asymptotic behavior of p_K beyond 2.2 $R_\odot$. The radiance maps of the K corona can then be derived.

References

Abbott, W.N.: 1955, Variation of the absolute surface brightness in the corona with the solar cycle. *Ann. Astrophys.* **18**, 81. ADS.

Allen, C.W.: 1973, *Astrophysical Quantities*, 3rd edn. Athlone Press, London, 176. ADS.

Altrock, R.C.: 2013, Forecasting the maxima of solar cycle 24 with coronal Fe XIV emission. *Solar Phys.* **289**, 623. DOI.

Ball, W.T., Unruh, Y.C., Krivova, N.A., Solanki, S., Wenzler, T., Mortlock, D.J., Jaffe, A.H.: 2012, Reconstruction of total solar irradiance 1974 – 2009. *Astron. Astrophys.* **541**, A27. DOI.

Basu, S., Broomhall, A.M., Chaplin, W.J., Elsworth, Y.: 2012, Thinning of the Sun's magnetic layer: The peculiar solar minimum could have been predicted. *Astrophys. J.* **758**, 43. DOI.

Bazilevskaya, G.A., Broomhall, A.-M., Elsworth, Y., Nakariakov, V.M.: 2014, A combined analysis of the observational aspects of the quasi-biennial oscillation in solar magnetic activity. *Space Sci. Rev.* **186**, 359. DOI.

Benevolenskaya, E.E.: 1998, A model of the double magnetic cycle of the Sun. *Astrophys. J.* **509**, L49. DOI.

Benevolenskaya, E.E., Kostuchenko, I.G.: 2013, The total solar irradiance, UV emission and magnetic flux during the last solar cycle minimum. *J. Astrophys.* **2013**, 368380. ADS.

Benevolenskaya, E.E., Slater, G., Lemen, J.: 2003, Impulses of activity and the solar cycle. *Solar Phys.* **216**, 325. DOI.

Benevolenskaya, E.E., Slater, G., Lemen, J.: 2014, Synoptic solar cycle 24 in corona, chromosphere, and photosphere seen by the solar dynamics observatory. *Solar Phys.* **289**, 3371. DOI.

Bisoi, S.K., Janardhan, P., Chakrabarty, D., Ananthakrishnan, S., Divekar, A.: 2014, Changes in quasi-periodic variations of solar photospheric fields: Precursor to the deep solar minimum in cycle 23? *Solar Phys.* **289**, 41. DOI.

Brueckner, G.E., Howard, R.A., Koomen, M.J., Korendyke, C.M., Michels, D.J., Moses, J.D., Socker, D.G., Dere, K.P., Lamy, P.L., Llebaria, A., Bout, M.V., Schwenn, R., Simnett, G.M., Bedford, D.K., Eyles, C.J.: 1995, The Large Angle Spectroscopic Coronagraph (LASCO). *Solar Phys.* **162**, 357. DOI.

Chowdhury, P.: 2011, Periodic behavior of solar electron flares during descending phase of cycle 23. *Proc. 32nd Int. Cosmic Ray Conf.* **10**, 132. DOI.

Chowdhury, P., Dwivedi, B.N.: 2011, Periodicities of sunspot number and coronal index time series during solar cycle 23. *Solar Phys.* **270**, 365. DOI.

Dikpati, M.: 2011, Comparison of the past two solar minima from the perspective of the interior dynamics and dynamo of the Sun. *Space Sci. Rev.* **176**, 279. DOI.

Dikpati, M., Gilman, P.A., de Toma, G., Ulrich, R.K.: 2010, Impact of changes in the Sun's conveyor-belt on recent solar cycles. *Geophys. Res. Lett.* **37**, 14107. DOI.

Fisher, R., Sime, D.G.: 1984, Solar activity cycle variation of the K corona. *Astrophys. J.* **285**, 354. DOI.

Frick, P., Galyagin, D., Hoyt, D.V., Nesme-Ribes, E., Schatten, K.H., Sokoloff, D., Zakharov, V.: 1997, Wavelet analysis of solar activity recorded by sunspot groups. *Astron. Astrophys.* **328**, 670. ADS.

Fröhlich, C.: 2013, Total solar irradiance: What have we learned from the last three cycles and the recent minimum? *Space Sci. Rev.* **176**, 237. DOI.

Gardès, B., Lamy, P., Llebaria, A.: 2013, Photometric calibration of the LASCO-C2 coronagraph over 14 years (1996 – 2009). *Solar Phys.* **283**, 667. DOI.

Gopalswamy, N., Yashiro, S., Mäkelä, P., Michalek, G., Shibasaki, K., Hathaway, D.H.: 2012, Behavior of solar cycles 23 and 24 revealed by microwave observations [Erratum: doi:10.1088/2041-8205/763/1/L24]. *Astrophys. J. Lett.* **750**, L42. DOI.

Grinsted, A., Moore, J.C., Jevrejeva, S.: 2004, Application of the cross wavelet transform and wavelet coherence to geophysical time series. *Nonlinear Proc. Geophys.* **11**, 561.

Hathaway, D.H.: 2010, The solar cycle. *Living Rev. Solar Phys.* **7**(1). DOI.

Howe, R., Christensen-Dalsgaard, J., Hill, F., Komm, R.W., Larsen, R.M., Schou, J., Thompson, M.J., Toomre, J.: 2000, Dynamic variations at the base of the solar convection zone. *Science* **287**, 2456. DOI.

Howe, R., Christensen-Dalsgaard, J., Hill, F., Komm, R., Schou, J., Thompson, M.J., Toomre, J.: 2007, Temporal variations in the solar rotation at the bottom of the convection zone: The current status. *Adv. Space Res.* **40**, 915. DOI.

Kilcik, A., Ozguc, A., Yurchyshyn, V., Rozelot, J.P.: 2014, Sunspot count periodicities in different Zurich sunspot group classes since 1986. *Solar Phys.* **289**, 4365. DOI.

Krivodubskij, V.N.: 2005, Turbulent dynamo near tachocline and reconstruction of azimuthal magnetic field in the solar convective zone. *Astron. Nachr.* **326**, 61. DOI.

Krivova, N.A., Solanki, S.K.: 2002, The 1.3-year and 156-day periodicities in sunspot data: Wavelet analysis suggests a common origin. *Astron. Astrophys.* **394**, 701. DOI.

Krivova, N.A., Solanki, S.K., Fligge, M., Unruh, Y.C.: 2003, Reconstruction of solar irradiance variations in cycle 23: Is solar surface magnetism the cause? *Astron. Astrophys.* **399**, L1. DOI.

Lamy, P., Llebaria, A., Quémerais, E.: 2002, Solar cycle variation of the radiance and the global electron density of the solar corona. *Adv. Space Res.* **29**, 373. DOI.

Lamy, P., Barlyaeva, T., Llebaria, A., Floyd, O.: 2014, Comparing the solar minima of cycles 22/23 and 23/24: The view from LASCO white-light coronal images. *J. Geophys. Res.* **119**, 47. DOI.

Lean, J.: 1990, Evolution of the 155 day periodicity in sunspot areas during solar cycles 12 to 21. *Astrophys. J.* **363**, 718. DOI.

Lean, J.L., Brueckner, G.E.: 1989, Intermediate-term solar periodicities: 100 – 500 days. *Astrophys. J.* **337**, 568. DOI.

Lebecq, C., Koutchmy, S., Stellemacher, G.: 1985, The 1981 total solar eclipse corona. II. Global absolute photometric analysis. *Astron. Astrophys.* **152**, 157. ADS.

Llebaria, A., Lamy, P.: 2008, In-orbit calibration of the polarization flat fields of the SOHO-LASCO coronagraphs. In: Oschmann, J.M. Jr., de Graauw, M.W.M., MacEwen, H.A. (eds.) *Space Telescopes and Instrumentation 2008: Optical, Infrared, and Millimeter*, *Proc. SPIE* **7010**, 70101I. DOI.

Llebaria, A., Lamy, P., Bout, M.V.: 2004, Lessons learned from the SOHO/LASCO-C2 calibration. In: Fineschi, S., Grumman, M.A. (eds.) *Telescopes and Instrumentation for Solar Astrophysics*, *Proc. SPIE* **5171**, 26. DOI.

Llebaria, A., Lamy, P., Danjard, J.-F.: 2006, Photometric calibration of the LASCO-C2 coronagraph for solar system objects. *Icarus* **182**, 281. DOI.

Llebaria, A., Lamy, P., Koutchmy, S.: 1999, The global activity of the solar corona. In: Vial, J.-C., Kaldeich-Schümann, B. (eds.) *Proc. 8th SOHO Workshop, Plasma Dynamics and Diagnostics in the Solar Transition Region and Corona*, *ESA SP-466*, 441. ADS.

Llebaria, A., Loirat, J., Lamy, P.: 2010, Restitution of multiple overlaid components on extremely long series of solar corona images. In: Bouman, C.A., Pollak, I., Wolfe, P.J. (eds.) *Computational Imaging VIII*, *Proc. SPIE* **7533**, 75330I. DOI.

Llebaria, A., Thernisien, A.F.R.: 2001, Highly accurate photometric equalization of long sequences of coronal images. In: Starck, J.-L., Murtagh, F.D. (eds.) *Astronomical Data Analysis*, *Proc. SPIE* **4477**, 265. DOI.

Lou, Y.-Q.: 2000, Rossby-type wave-induced periodicities in flare activities and sunspot areas or groups during solar maxima. *Astrophys. J.* **540**, 1102. DOI.

Maraun, D., Kurths, J.: 2004, Cross wavelet analysis: Significance testing and pitfalls. *Nonlinear Proc. Geophys.* **11**, 505. DOI.

McIntosh, S.W., Leamon, R.J., Gurman, J.B., Olive, J.-P., Cirtain, J.W., Hathaway, D.H., Burkepile, J., Miesch, M., Markel, R.S., Sitongia, L.: 2013, Hemispheric assymmetries of solar photospheric magnetism: Radiative, particulate, and heliospheric impacts. *Astrophys. J.* **765**, 146. DOI.

Mendoza, B., Velasco, V.M., Valdés-Galicia, J.F.: 2006, Mid-term periodicities in the solar magnetic flux. *Solar Phys.* **233**, 319. DOI.

Nair, V.S., Nayar, S.R.P.: 2008, North–South asymmetry in solar wind & geomagnetic activity and its solar cycle evolution. *Indian J. Radio Space Phys.* **37**, 391.

Nikonov, V.B., Nikonova, E.K.: 1947, *Izv. Krym. Astrofyz. Obs.* **1**, 83.

Oliver, R., Ballester, J.L.: 1996, Rescaled range analysis of the asymmetry of solar activity. *Solar Phys.* **169**, 215. DOI.

Oliver, R., Ballester, J.L., Baudin, F.: 1998, Emergence of magnetic flux on the Sun as the cause of a 158-day periodicity in sunspot areas. *Nature* **394**, 552. DOI.

Ostryakov, V.M., Usoskin, I.G.: 1990, Correlation dimensions of structured signals. *Sov. Tech. Phys. Lett.* **16**, 658.

Pagot, E., Lamy, P., Llebaria, A., Boclet, B.: 2013, Automated processing of LASCO coronal images: Spurious point-source filtering and missing blocks correction. *Solar Phys.* **289**, 1433. DOI.

Petrie, G.J.D.: 2012, Evolution of active and polar photospheric magnetic fields during the rise of cycle 24 compared to previous cycles. *Solar Phys.* **281**, 577. DOI.

Rieger, E., Share, G.H., Forrest, D.J., Kanbach, G., Reppin, C., Chupp, E.L.: 1984, A 154-day periodicity in the occurrence of hard solar flares? *Nature* **312**, 623. DOI.

Saito, K.: 1950, Brightness and polarization of the solar corona. *Ann. Tokyo Astron. Obs., 2nd Ser.*, **3**, 3. ADS.

Sturrock, P.A., Scargle, J.D., Walther, G., Wheatland, M.S.: 1999, Rotational signature and possible r-mode signature in the GALLEX solar neutrino data. *Astrophys. J. Lett.* **523**, L177. DOI.

Sytinskaya, N.N., Sharonov, V.V.: 1983, In: Evans, J. (ed.) *The Solar Corona*, Academic Press, New York, 301.

Tappin, S.J., Altrock, R.C.: 2013, The extended solar cycle tracked high into the corona. *Solar Phys.* **282**, 249. DOI.

Tapping, K.F.: 2006, Solar activity indices. In: Murdin, P. (ed.) *Encyclopedia of Astronomy & Astrophysics*. http://eaa.crcpress.com.

Tapping, K.F., Boteler, D., Charbonneau, P., Crouch, A., Manson, A., Paquette, H.: 2007, Total magnetic activity and total irradiance since the Maunder minimum. *Solar Phys.* **246**, 309. DOI.

Telloni, D., Ventura, R., Romano, P., Spadaro, D., Antonucci, E.: 2013, Detection of plasma fluctuations in white-light images of the outer solar corona: Investigation of the spatial and temporal evolution. *Astrophys. J.* **767**, 138. DOI.

Torrence, C., Compo, G.P.: 1998, A practical guide to wavelet analysis. *Bull. Am. Meteorol. Soc.* **79**, 61. ADS.

Usoskin, I.G.: 2013, A history of solar activity over millennia. *Living Rev. Solar Phys.* **10**(1). DOI.

van de Hulst, H.C.: 1950, The electron density of the solar corona. *Bull. Astron. Inst. Neth.* **11**, 135. ADS.

Waldmeier, M.: 1955, Ergebnisse der Zürcher sonnenfinsternisexpedition 1954. I. Vorläufige photometrie der korona. *Z. Astrophys.* **36**, 275. ADS.

Wang, Y.-M., Robbrecht, E., Sheeley, N.R. Jr.: 2009, On the weakening of the polar magnetic fields during solar cycle 23. *Astrophys. J.* **707**, 1372. DOI.

Wang, Y.-M., Sheeley, N.R. Jr.: 2003, On the fluctuating component of the Sun large-scale magnetic field. *Astrophys. J.* **590**, 1111. DOI.

Wolff, C.L.: 1983, The rotational spectrum of g-modes in the Sun. *Astrophys. J.* **264**, 667. DOI.

Zolotova, N.V., Ponyavin, D.I., Arlt, R., Tuominen, I.: 2010, Secular variation of hemispheric phase differences in the solar cycle. *Astron. Nachr.* **331**, 765. DOI.